

UKAEA FUS 432

EURATOM/UKAEA Fusion

**Equilibrium reconstruction in the
START tokamak**

L C Appel, M K Bevir and M J Walsh

August 2000

© UKAEA

EURATOM/UKAEA Fusion Association

Culham Science Centre, Abingdon
Oxfordshire, OX14 3DB
United Kingdom
Telephone +44 1235 463330
Facsimile +44 1235 463647

Equilibrium reconstruction in the START tokamak

L.C. APPEL, M.K. BEVIR, M.J. WALSH[†]

EURATOM/UKAEA Fusion Association, Culham Science Centre, Abingdon, Oxon, OX14 3DB, United Kingdom.

[†] Walsh Scientific Limited, Culham Science Centre, Abingdon, Oxon, OX14 3EB.

Abstract. The computation of magnetic equilibria in the START spherical tokamak is more difficult than in more conventional large aspect ratio tokamaks. This difficulty arises partly as a result of the use of induction compression to generate high-current plasma as this precludes the positioning of magnetic diagnostics close to the outboard side of the plasma. In addition, the effect of a conducting wall with a high, but finite, conductivity must be included. This paper presents a method for obtaining plasma equilibrium reconstructions based on the EFIT code. New constraints are used to relate iso-flux surface locations deduced from radial profile measurements of electron temperature. A model of flux diffusion through the vessel wall is developed. It is shown that neglecting flux diffusion in the vessel wall can lead to a significant underestimate in the calculation of the plasma β_t . Using a relatively sparse set of magnetic signals, β_t can be obtained to within a fractional error of $\pm 10\%$. Using constraints to relate iso-flux surface locations the principal of determining the internal q-profile is demonstrated.

1. Introduction

A knowledge of the magnetic configuration satisfying equilibrium force balance is an essential starting point for a detailed assessment of plasma performance in a tokamak. The governing equation is usually taken to be the Grad-Shafranov equation [1–7], although extensions to this equation to take account of plasma pressure anisotropy and bulk plasma rotation have also been considered [8–10]. Constraints on determining experimental equilibria are provided by a set of magnetic field detectors and flux loops arranged around the vessel, possibly interpolated to yield continuous functions of both poloidal flux ψ_p and its normal derivative $\underline{n} \cdot \nabla \psi_p$ around the plasma. In these terms, the problem consists of solving an elliptic equation subject to Cauchy boundary conditions and is ill-posed, i.e. small perturbations in the boundary propagate to produce large changes in the solution a short distance away from the measuring contour [11, page 702].

The ill-posed nature of the problem can be overcome by restricting the choice of the source functions [11, page 1276]. A common practice is to define the plasma functions as apolynomial functions with coefficients to be determined during the reconstruction process. With the plasma current distribution represented by sufficiently few degrees of freedom, it is possible to design a magnetic reconstruction algorithm which is robust yet accurate. The problem is that the class of permissible current profiles may be far from the actual magnetic configuration and one must seek a compromise between achieving a robust algorithm and not overly restricting the permissible class of current profiles.

This paper reports on work carried out to reconstruct magnetic equilibria in the START spherical tokamak. The reconstructions used the EFIT code [2] which has been employed extensively on many other tokamak experiments, including DIII-D [12], JET [13], and more recently the COMPASS-D and START tokamaks. There are two distinct features of START that complicate attempts to carry out equilibrium reconstructions. The first arises from the use of induction-compression [14] to generate high-performance plasmas at low aspect ratio which precludes positioning magnetic diagnostics close to the outboard side of the plasma. The second arises from the presence of a conducting wall with high, but finite, conductivity. This paper discusses

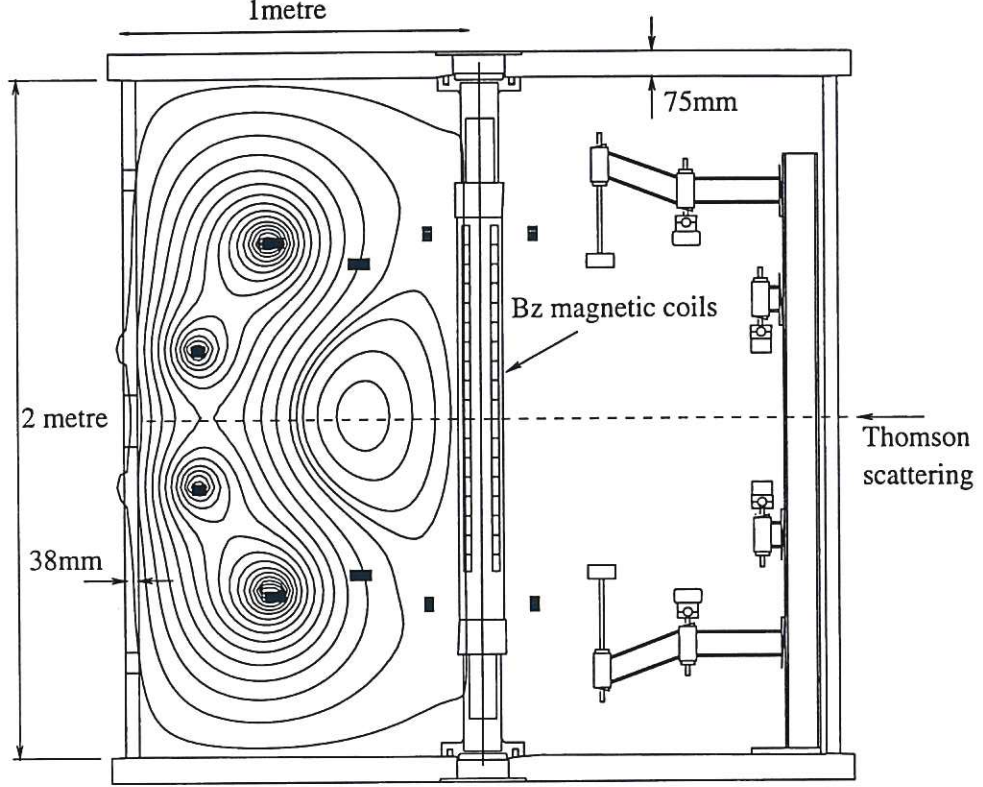


Figure 1. location of START coils and diagnostics

how these complications have been overcome by the implementation of a model for flux diffusion into the vessel and by the use of constraints to fix the locations of iso-poloidal flux surfaces.

Figure 1 shows a cross-section of START. The plasma forms inside a vacuum tank made of aluminium alloy with thicknesses of 3.8cm on the vertical walls and 7.5cm on the two ends. The poloidal field coils are situated within the tank. The outer two pairs, referred to later as BV coils, produce the dominant vertical field. The inner coil pair is for the formation of diverter plasma configurations, and the remaining coil pair is used during plasma formation prior to compression. An array of 46 discrete magnetic coils measuring the vertical magnetic field are located on the central solenoid, and this is screened by a thin central stainless steel tube 3mm thick and a graphite limiter with an outer diameter of 130mm. Rogowskii coils measure current in the poloidal field coils and in the plasma. The electron temperature and density profiles, T_e and n_e respectively, are measured with a multi-point Thomson scattering system along the horizontal mid-plane [15]. The system is calibrated using a HCN interferometer with a radial chord on the mid-plane, inwardly directed and reflected off the centre column. Ion temperatures are obtained from charge exchange spectra [16]. In addition there are two SXR diode arrays with horizontal and vertical views to provide information on the radius of the $q=1$ surface when the discharge is sawtoothing (here q is the safety factor).

In the following section we summarize the EFIT algorithm and describe a new constraint to equalise poloidal flux at pairs of user-defined locations. In section 3. a model is developed to predict flux diffusion through the START vessel wall. Finally, in section 4., the method of obtaining equilibrium reconstructions is described, with several illustrative examples.

2. The EFIT algorithm

The EFIT code solves the equation for equilibrium force balance, the Grad-Shafranov equation, subject to multiple constraints that may be expressed in a large variety of ways. Mathematically, the Grad-Shafranov equation can be written,

$$\Delta^* \psi_p = -\mu_0 R J_\phi(R, Z) \quad (2..1)$$

where

$$\Delta^* = R \frac{\partial}{\partial R} \frac{1}{R} \frac{\partial}{\partial R} + \frac{\partial^2}{\partial z^2} \quad (2..2)$$

and $J_\phi(R, Z)$ is the toroidal current density which can be written in terms of the flux functions $p(\psi_p)$ and $f(\psi_p)$ (respectively, the plasma pressure and RB_ϕ):

$$J_\phi(R, Z) = R p' + \frac{1}{\mu_0 R} f f' \quad (2..3)$$

in which ' denotes $\partial/\partial\psi_p$. The current in the poloidal field coils is represented as a set of coefficients $I_i^{pf}, i = 1, \dots, N_c$. The current in the plasma is expressed as

$$J_\phi(R, Z)^{plasma} = R \sum_{i=0}^{N_\alpha-1} \alpha_i c_i(\psi_p) + \frac{1}{\mu_0 R} \sum_{i=0}^{N_\gamma-1} \gamma_i d_i(\psi_p) \quad (2..4)$$

where $c_i(\psi_p), i = 0, \dots, N_\alpha - 1$, $d_i(\psi_p), i = 0, \dots, N_\gamma - 1$, are basis functions specified at run time from a choice that currently includes polynomial functions and tension splines [17].

Equation (2..1) is solved iteratively, using the previous solution for ψ_p to update equation (2..4). A finite difference scheme is used to obtain the contribution of the plasma current using a regular grid consisting of N_p cells, each of area δA . To enhance numerical accuracy, contributions from the poloidal field coil currents are obtained using precomputed Green's functions. Interleaved between each iteration, EFIT computes updated values of the coefficients, $\alpha_i (i = 0, \dots, N_\alpha - 1)$, $\gamma_i (i = 0, \dots, N_\gamma - 1)$, $I_i^{pf} (i = 1, \dots, N_c)$, (using the field solution of the previous iteration) to provide a best-fit to the user-imposed constraints. The constraints are expressed in linearised form, the representation for the k^{th} constraint being

$$a_P^k = a_0^k + \sum_{i=0}^{N_\alpha-1} \frac{\partial a^k}{\partial \alpha_i} \alpha_i + \sum_{i=0}^{N_\gamma-1} \frac{\partial a^k}{\partial \gamma_i} \gamma_i + \sum_{i=1}^{N_c} \frac{\partial a^k}{\partial I_i^{pf}} I_i^{pf} \quad (2..5)$$

where a_P^k is the value of the constraint as computed by EFIT. The k^{th} constraint equation is obtained by equating a_P^k with the user-supplied target value a_M^k :

$$\sum_{i=0}^{N_\alpha-1} \frac{\partial a^k}{\partial \alpha_i} \alpha_i + \sum_{i=0}^{N_\gamma-1} \frac{\partial a^k}{\partial \gamma_i} \gamma_i + \sum_{i=1}^{N_c} \frac{\partial a^k}{\partial I_i^{pf}} I_i^{pf} = (a_M^k - a_0^k) \quad (2..6)$$

The assembled system of equations, weighted to reflect the accuracy of the data, is solved using the singular value decomposition method [18].

In addition to the constraints already existing in EFIT, a new constraint has been implemented enabling the poloidal flux values at one or more pairs of user-defined locations \mathbf{X}_{M_1} and \mathbf{X}_{M_2} to be equated. Writing the constraint $a = \psi_p(\mathbf{X}_{M_1}) -$

$\psi_p(\mathbf{X}_{M_2})$, expressions for the coefficients of the above equations are

$$a_0 = 0 \quad (2..7)$$

$$\frac{\partial a}{\partial I_i^{pf}} = \frac{\partial \psi(\mathbf{X}_{M_1})}{\partial I_i^{pf}} - \frac{\partial \psi(\mathbf{X}_{M_2})}{\partial I_i^{pf}} \quad (2..8)$$

$$\frac{\partial a}{\partial \alpha_i} = \sum_{j=1}^{N_p} R_j c_i(\psi_p(\mathbf{X}_j)) \delta A \left(\frac{\partial \psi(\mathbf{X}_{M_1})}{\partial I(\mathbf{X}_j)} - \frac{\partial \psi(\mathbf{X}_{M_2})}{\partial I(\mathbf{X}_j)} \right) \quad (2..9)$$

$$\frac{\partial a}{\partial \gamma_i} = \sum_{j=1}^{N_p} \frac{d_i(\psi_p(\mathbf{X}_j)) \delta A}{\mu_o R_j} \left(\frac{\partial \psi(\mathbf{X}_{M_1})}{\partial I(\mathbf{X}_j)} - \frac{\partial \psi(\mathbf{X}_{M_2})}{\partial I(\mathbf{X}_j)} \right) \quad (2..10)$$

Note that $\frac{\partial \psi(\mathbf{X}_i)}{\partial I(\mathbf{X}_j)}$ is the poloidal flux at \mathbf{X}_i due to a unit toroidal current at \mathbf{X}_j .

3. Flux diffusion through the START vessel wall

Over the duration of a START discharge, typically 20-25msec, the vessel wall acts as an imperfect flux conserver with a small but measurable flux ($\approx 8\text{mWb}$) diffusing through it. In the absence of sufficient magnetic diagnostics to quantify the induced eddy currents, a model has been developed to predict the flux penetration through the wall.

The equation for poloidal flux evolution in the START vessel (assumed to be axisymmetric and homogeneous) is

$$\nabla^2 \psi_p = \mu \sigma \frac{\partial \psi_p}{\partial t} \quad (3..1)$$

where μ is magnetic permeability and σ is the vessel conductivity. Considering only the diffusion of flux normal to the wall, the equation reduces to

$$\frac{\partial^2 \psi_p}{\partial x^2} = \mu \sigma \frac{\partial \psi_p}{\partial t} \quad (3..2)$$

where x is in the direction perpendicular to the wall, and it is assumed that $d \ll L$ (d is wall thickness, L is global dimension).

In developing a model for START, the tangential magnetic field $B(t)$ at the inner wall surface is taken to be a known function of time. The behaviour of the diffusing flux is most clearly understood by examining the particular situation in which, at $t=0$, a constant radial flux gradient (tangential field), $G = \partial \psi_p / \partial x = RB(t)$, is applied on the inner wall of the vessel ($x=0$). Initially, flux diffuses into the wall unaffected by the presence of the outer boundary. The variation of flux can be expressed [19, page 75]

$$\begin{aligned} \psi_p(x, t) = 2G \left(\sqrt{\frac{t}{\pi \mu \sigma}} \exp \left\{ -\frac{x^2 \mu \sigma}{4t} \right\} \right. \\ \left. - \frac{x}{2} \operatorname{erfc} \left\{ \frac{x}{2} \sqrt{\frac{\mu \sigma}{t}} \right\} \right) \end{aligned} \quad (3..3)$$

where x is now the distance from the surface of the inner wall. A useful measure of flux penetration is the effective skin depth, δ , defined as the depth at which $\psi_p = 0$, assuming the poloidal flux decreases linearly from the inner wall with gradient G , and with $\psi_p(x=0)$ given by equation (3..3):

$$\delta = \sqrt{\frac{4t}{\pi \mu \sigma}} \quad (3..4)$$

This expression is similar to the more usual definition of skin-depth defined for a field oscillating sinusoidally at angular frequency ω [20]:

$$\delta = \sqrt{2\mu\omega\sigma} \quad (3.5)$$

For $t \gtrsim \mu\sigma d^2$, the flux will have diffused to the outer boundary ($d \approx \delta$) and equation (3.3) becomes invalid. Assuming $\partial\psi_p/\partial x(x=d) = 0$ so the field at the external wall is zero, the poloidal flux is [19, page 112]

$$\begin{aligned} \psi_p(x, t) = & \frac{Gt}{\mu\sigma d} + Gd \left(\frac{3(d-x)^2 - d^2}{6d^2} - \frac{2}{\pi^2} \sum_{n=1}^{\infty} \frac{(-1)^n}{n^2} \right. \\ & \left. \exp\left(\frac{-n^2\pi^2 t}{\mu\sigma d^2}\right) \cos \frac{n\pi(d-x)}{d} \right) \end{aligned} \quad (3.6)$$

An upper limit, t_L , for the applicability of this assumption can be made as follows. For very long times, the flux difference across the wall is insignificant, and the flux on the outer and inner surfaces is approximately the same, given by the first term of equation (3.6)

$$\psi_p = \frac{Gt_L}{\mu\sigma d} \quad (3.7)$$

The radial flux gradient is $G \approx \psi_p/L$, yielding

$$t_L = \mu\sigma dL \quad (3.8)$$

An estimate of t_L for the START wall using $\sigma = 1.85 \times 10^7 \Omega^{-1}\text{m}^{-1}$, $\mu = 4\pi \times 10^{-7}$, $d = 5\text{cm}$, $L = 1\text{m}$ gives $t_L \approx 1\text{sec}$, considerably larger than the START discharge time ($\approx 20\text{ms}$), and hence equation (3.6) is applicable for START conditions.

The toroidal current density within the vessel wall can be expressed

$$J_{wall}(x, t) = \frac{\sigma}{\mu R} \frac{\partial\psi_p(x, t)}{\partial t} \quad (3.9)$$

The evolution of poloidal flux for an arbitrary time-variation of tangential magnetic field incident on the inner wall can be obtained by first decomposing $G(t)$ into a sum of Heaviside functions:

$$G(t) = \sum_{n=1}^m H(t - t_n) G_n \quad (3.10)$$

The poloidal flux is then

$$\psi_{p[TOTAL]}(x, t) = \sum_{n=1}^m \psi_p(x, t - t_n) G_n H(t - t_n) \quad (3.11)$$

where ψ_p is obtained from equation (3.6). In the appendix some simple formulae for the flux and the effective skin-depth are given which are valid for short and long time-scales.

4. Implementation of EFIT for START

The external magnetic signals provide a starting point for all equilibrium calculations. Figure 1 shows the location of the 46 magnetic detectors on the centre column measuring the vertical magnetic field. Currents flowing in the poloidal field coils and induced in their conductive metal casings are measured by Rogowskii coils. In addition there is a full Rogowskii coil for measuring the plasma current and a diamagnetic loop.

The two arrays of SXR diodes are available to provide the location of the sawtooth inversion radius, likely to be close to the $q=1$ surface, and the magnetic axis (assumed to be at the radius of peak emission). Measurements of T_e and n_e are obtained from Thomson scattering at 29 radial locations across the mid-plane at a single time point in each discharge. By assuming high parallel electron heat conduction, the radial profile of T_e can be used as relational constraints on flux surfaces inboard and outboard of the magnetic axis. To facilitate this, a new constraint to equalize poloidal flux values, described in section 2., has been implemented in EFIT. Measurements of T_e , n_e and thermal ion temperature T_i from charge exchange measurements provide the kinetic thermal pressure. The fast ion component can be computed using the Monte-Carlo particle tracking code LOCUST [21].

In setting up EFIT to carry out reconstructions on START, the vacuum vessel is divided into 148 discrete elements which can each carry a uniform current. On the inner surface of each element a virtual flux loop is defined to control the poloidal flux values on the inner surface of the vacuum vessel. To obtain an equilibrium reconstruction, EFIT is run in two stages. In the first stage, the vessel is treated as a perfect flux conserver by constraining the flux on the vessel wall to zero. EFIT runs are performed over the duration of the discharge and the time-variation of the tangential magnetic field computed at each of the virtual vessel flux loop locations. Using these values, the poloidal flux at each of the flux loop locations is computed from equation (3.11). EFIT is then run for a second time, fitting to the updated poloidal flux values on the vessel wall. Although the poloidal flux at the wall could, in principle, be computed again, further iterations were found to be unnecessary.

4.1. Calculations in the absence of plasma

To verify the wall model, the procedure outlined in the previous section was used to reconstruct discharge 35345 with typical externally driven current waveforms, but with a conducting plasma absent. A series of runs was carried out with a range of wall conductivities in which the central magnetic detectors were not used as constraints. Figure 2 shows the time evolution of measured and predicted fields for the mid-plane magnetic detector on the centre tube. With zero flux penetration into the wall, the predicted magnetic field is $\sim 15\%$ less than measured at $t=40\text{ms}$, close to when peak plasma performance would be expected. Results for other magnetic detectors are shown in figure 3 for $t=40\text{ms}$, and are similar. Using a conductivity $\sigma = 1.85 \times 10^7 \Omega^{-1}\text{m}^{-1}$, gives a good match (to better than 1% for the central detectors). This value of σ will be used for the results presented later.

Figure 4 shows the evolution of the toroidal current within the vessel wall versus distance from the inner wall on the mid-plane predicted from equations (3.9) and (3.11). The poloidal field induction currents are applied at 21ms causing an induced current to appear instantaneously on the inner surface of the vessel. The current immediately begins to diffuse outwards, reaching the outer vessel edge by 26ms. The current on the inner wall continues to increase at a slower rate until $t=34\text{ms}$ in response to changing currents in the plasma compression coils. The figure shows that the induced current has diffused to the outer wall within 5ms of current initialization, and thereafter it rises rapidly. At $t=34\text{ms}$ at the time of peak current on the inner wall, $J_{\text{outer}}/J_{\text{inner}} = 54\%$, and between 40ms and 44ms the radial current profile is almost completely flat.

4.2. Equilibrium reconstruction of a plasma discharge

START discharge 36429 serves to illustrate the equilibrium reconstruction process. This is an ‘Ohmic H-mode’ discharge [22] and the reconstruction discussed here is

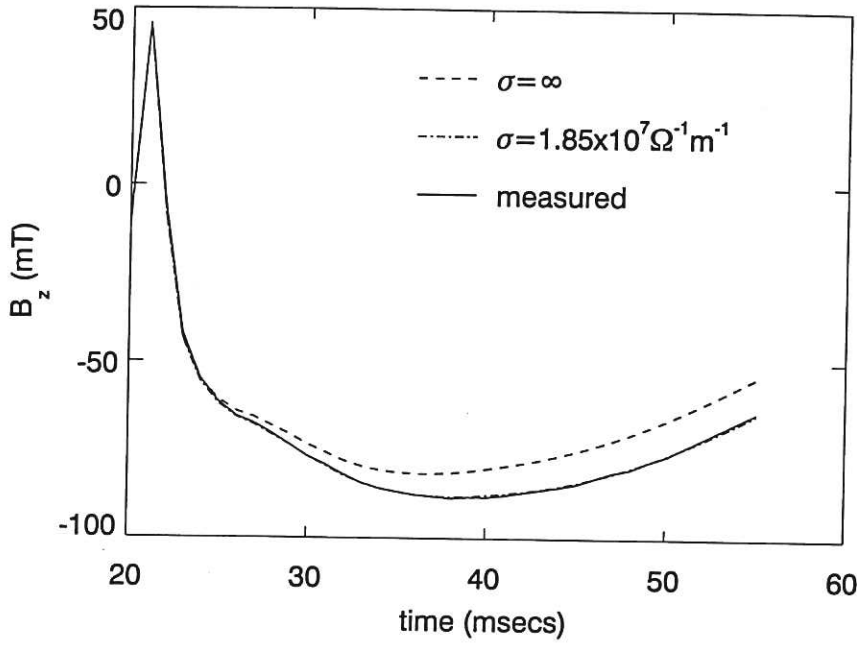


Figure 2. Time evolution of measured and predicted B_z signals on the inboard mid-plane for discharge 35345, for the perfectly conducting and resistive vessel.

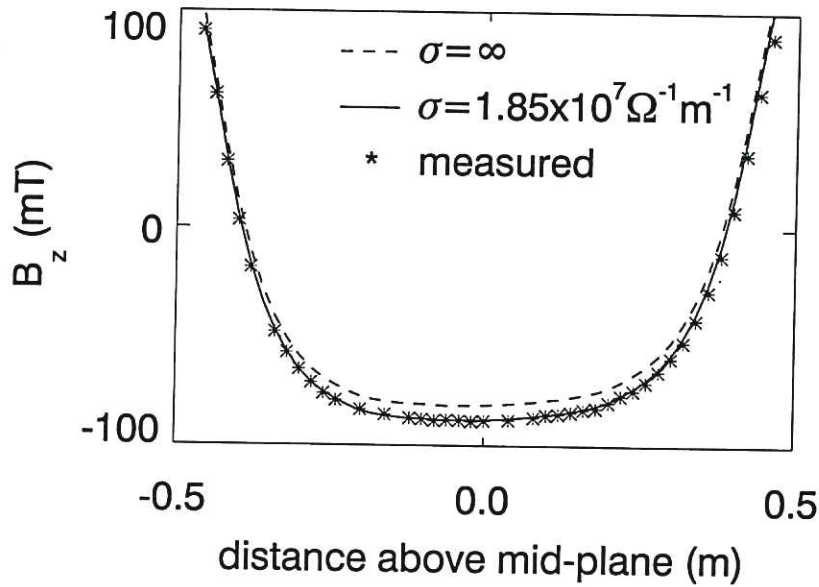


Figure 3. Measured and predicted B_z signals at $t=40\text{ms}$ for discharge 35345.

during the ELM phase at $t=41\text{ms}$. This is 6ms after neutral beam injection has ceased, by which time the energetic particles have thermalized. As shown in figure 5, this is during a quasi-steady state period with $I_p \approx 200\text{kA}$. Measurements of line-

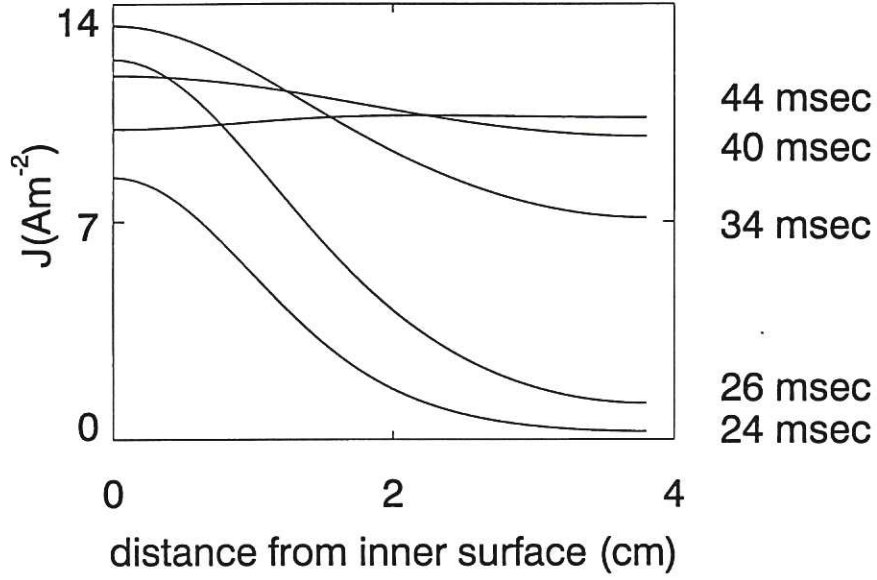


Figure 4. Computed radial profiles of the toroidal current in the vessel on the mid-plane for discharge 35345. (Note that the poloidal field currents are initialized at $t=21\text{ms}$.)

integrated density and SXR emission provide clear evidence of sawtooth activity from around 35ms. At this time, radial profiles of T_e and n_e are available from Thomson Scattering and $T_i = 220\text{eV}$ on axis (obtained from charge exchange measurements). In addition, the SXR emission indicates an inversion radius at around 41cm, giving an approximate radius for the $q=1$ surface. The SXR profile also indicates that the magnetic axis has a radius $R < 34.6\text{cm}$.

Initially, EFIT was run at 1ms intervals from $t=22\text{ms}$, immediately following the flux compression phase, fitting the measured poloidal field currents, plasma current and magnetic detector signals to within 5%, with the flux values on the wall constrained to zero. Subsequent runs of EFIT were at $t=41\text{ms}$ with the flux at the wall constrained to within $10\mu\text{Wb/rad}$ of the values computed using equation (3.11) and other magnetic signals fitted to within 5% of measured values (the magnitude of these signals ranged between 80mT and 350mT). Figure 6 shows the variation of $\beta_t = 2\mu_0 \langle p \rangle / B_o^2$ with q at the magnetic axis (where $\langle \dots \rangle$ denotes an average over the plasma volume and B_o is the vacuum toroidal field evaluated at the geometric axis). The calculations were carried out with EFIT fitting only to the measured magnetic signals, coil and plasma currents. The results show that $\beta_t \approx (9.5 \pm 1)\%$ using using several representations for the plasma flux functions p' and ff' (the precise representations are indicated in the figure).

The effect of flux diffusion into the vessel on β can be estimated in the following way. The conducting wall acts to modify the vertical field maintaining the radial force balance of the plasma. At large aspect ratio, the outward force of the plasma is given by [23, 24]

$$F_p = \frac{\mu_o I_p^2}{2} \left(\ln \frac{8R}{a} - \frac{3}{2} + \frac{l_i}{2} + \beta_p \right) \quad (4.1)$$

This is balanced by a force due to the external field, B_{ze} , resulting from currents in

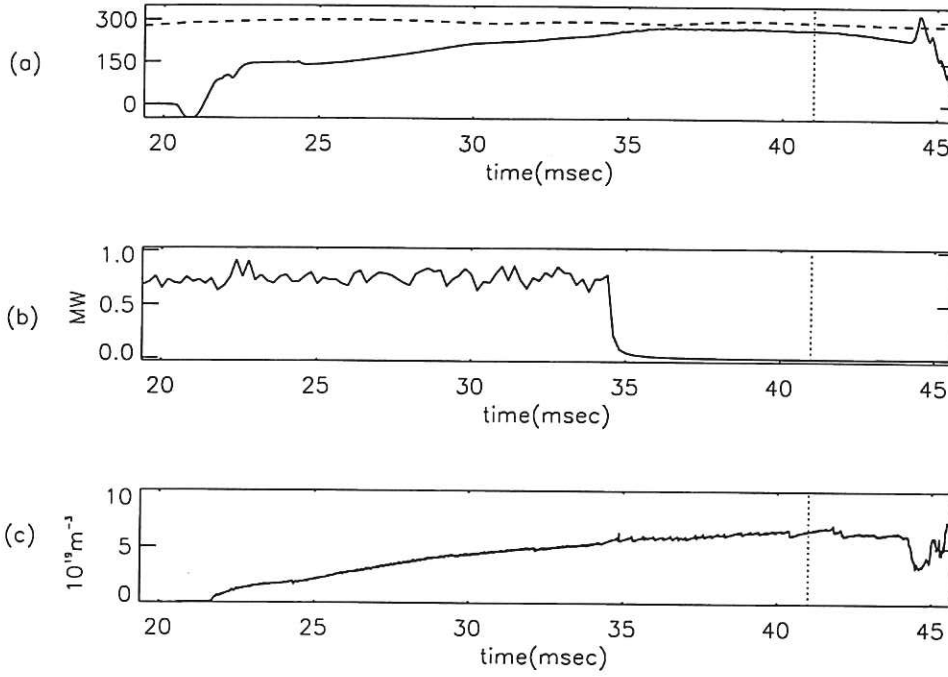


Figure 5. Details of START discharge 36429: (a) plasma current in kA, toroidal field at geometric axis in mT (dashed line); (b) neutral beam power; (c) line averaged density. The time ($t=41\text{ms}$) at which Thomson scattering data was obtained is shown, when the discharge is dominated by Ohmic heating.

poloidal field coils and induced currents in the wall

$$F_e = -2\pi B_{ze} I_p R \quad (4.2)$$

Figure 7 shows a graph of B_{ze} at $R=0.33\text{m}$, $Z=0\text{m}$ (the approximate location of the magnetic axis) with a flux-conserving wall moved between $\pm 10\text{cm}$ of the inner START wall position. The results were obtained with the poloidal field currents and plasma current measured at $t=41\text{msec}$. The plasma current was represented with a single filament at $R=0.33\text{m}$, $Z=0\text{m}$. The total external field is made up of two components arising from the poloidal field coil currents and from the plasma current. These are also plotted and show a competing effect with the contribution from the poloidal field coils increasing in magnitude as the wall is moved out whilst the contribution from the plasma current decreases. Equating (4.1) and (4.2), the variation of β_p with wall position can be obtained as shown in figure 8. Note that the result assumes invariance of R/a and l_i . For the experimental parameters, the effective skin depth on the vertical wall of START is (from equation A.12) $\delta(\text{cm}) = 1/(n+1)0.113t(\text{msec}) + 1.26$ where $B_s \propto t^n$ is the tangential magnetic field incident on the inner surface of the wall. At $t=20\text{msec}$, $\delta \leq 3.5\text{cm}$ for $n > 0$. This is equivalent to an outward movement by a distance δ of a flux-conserving wall. Thus, from figure 8, ignoring the effects of flux diffusion could result in an underestimate of β_p by ~ 0.08 . Since in START poloidal and toroidal fields are of the same magnitude, there will be a similar error on β_t .

Next, runs were carried out using the radial T_e profile to constrain the relative locations of poloidal flux surfaces at three pairs of points on the mid-plane: (i) $R=12\text{cm}$ and $R=50.2\text{cm}$; (ii) $R=16.5\text{cm}$ and $R=47.5\text{cm}$; and (iii) $R=21\text{cm}$ and $R=44\text{cm}$. Figure 9 shows the measured T_e radial profile onto which are mapped flux surface locations. The steep T_e gradient close to the edge means that it provides a strong constraint

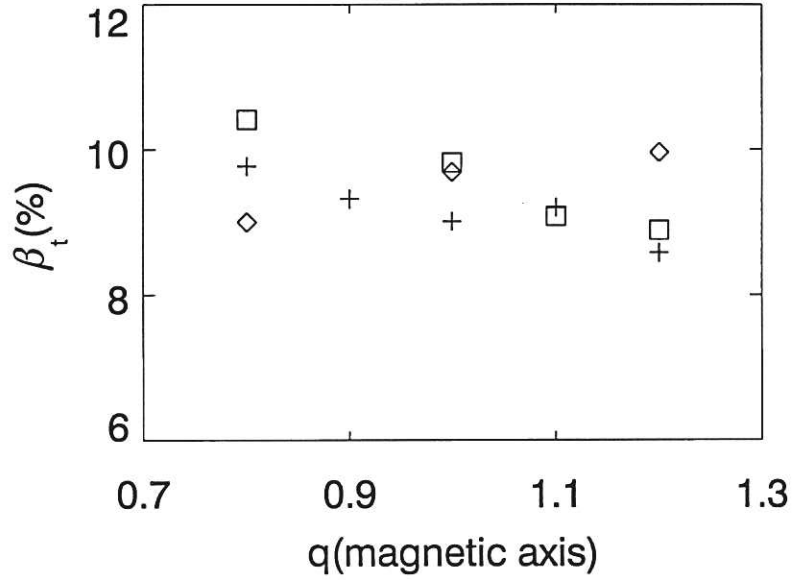


Figure 6. Results of EFIT reconstructions for discharge 36429 obtained using only the measured B_z signals on the centre column and measured coil currents. Plasma function representation is as follows: (+): $p' = a + b\bar{\psi}$, $ff' = c + d\bar{\psi}_p$; (\square): $p' = a + b\bar{\psi}$, $ff' = c$; (\diamond): $p' = a(1 - \bar{\psi}^2) + b(\bar{\psi} - \bar{\psi}^2)$, $ff' = c(1 - \bar{\psi})$. (Note that ' denotes $\partial/\partial\bar{\psi}$; also $\bar{\psi} = (\psi_p - \psi_o)/(\psi_b - \psi_o)$.)

on the outer flux surfaces (hence plasma volume) when the iso-flux constraint is applied, but not on the inner surfaces in the range $28\text{cm} \lesssim R \lesssim 40\text{cm}$. Figure 10 indicates the variation of β_t with q_0 . Error bars show the sensitivity to the results of applying 2% Gaussian noise to the magnetic data. These results were obtained using the following representation for the plasma functions: $p' = \sum_{i=0}^{i=1} a_i \bar{\psi}^i$, $ff' = \sum_{i=0}^{i=3} b_i \bar{\psi}^i$. Within these error bounds, the predicted value of $\beta_t = 8 \pm 1\%$, which is close to the range of values obtained above using no internal constraints, and it is insensitive to variations in q_0 . In principle, the value of q_0 can be deduced by finding the equilibrium solution which fits best to the data. Figure 11 shows the variation of χ^2 with q_0 , where $\chi^2 = \frac{1}{N} \sum \left(\frac{M_i - P_i}{2\% \times M_i} \right)^2$ in which M_i and P_i denote measured and predicted signals, respectively. The result indicates that q_0 is insensitive to variations in χ^2 which is in agreement with results reported previously [1]. Next, the sensitivity of q_0 to discrepancies in the flux values between each of the three pairs of relational constraint locations is examined. Figure 12 shows a scan of the average flux discrepancy $\delta\bar{\psi}_{FLUX}$ for $0.5 < q_0 < 1.4$. (The definition of $\delta\bar{\psi}_{FLUX}$ is $\sqrt{\sum_{i=1}^3 (\bar{\psi}_1^{(i)} - \bar{\psi}_0^{(i)})^2} / 3$ in which $\bar{\psi}_0^{(i)}$, $\bar{\psi}_1^{(i)}$ are, respectively, inboard and outboard predicted values of poloidal flux for the i^{th} relational constraint, normalized to 0 on the magnetic axis and to 1 on the separatrix.) The results, obtained in the absence of noise, indicates a minimum in $\delta\bar{\psi}_{FLUX}$ occurs around $q_0=0.7$. However, since the uncertainty in the position of constraint locations (as shown in figure 9) is at least 2cm, the uncertainty in normalized poloidal flux will be significantly higher than 2% and hence this value for q_0 cannot be substantiated.

The poloidal cross section of the solution with $q_0 = 0.9$ is shown in figure 13.

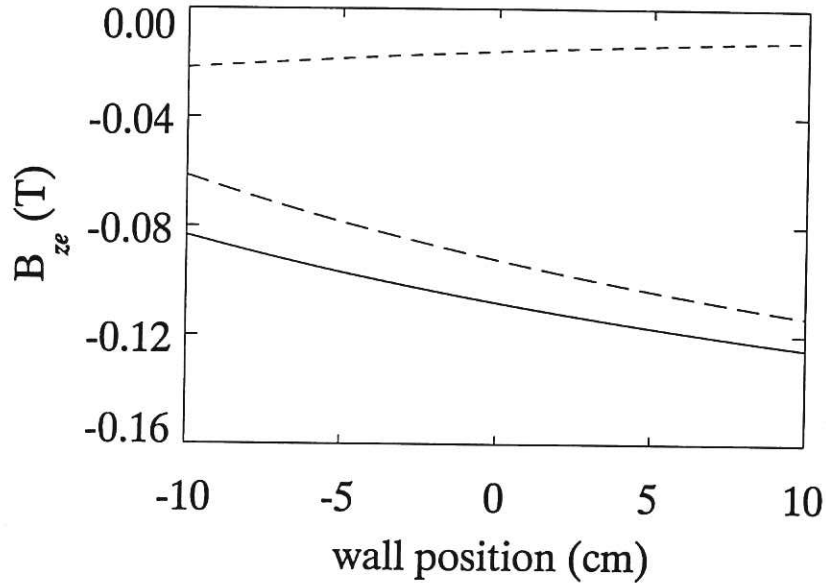


Figure 7. Calculated external magnetic field at $R=0.33\text{m}$, $Z=0\text{m}$ as a function of position of an ideal wall with respect to the inner surface of the actual resistive wall (solid line). The contributions resulting from the poloidal field coil currents (long dashes) and plasma current (short dashes) are also shown

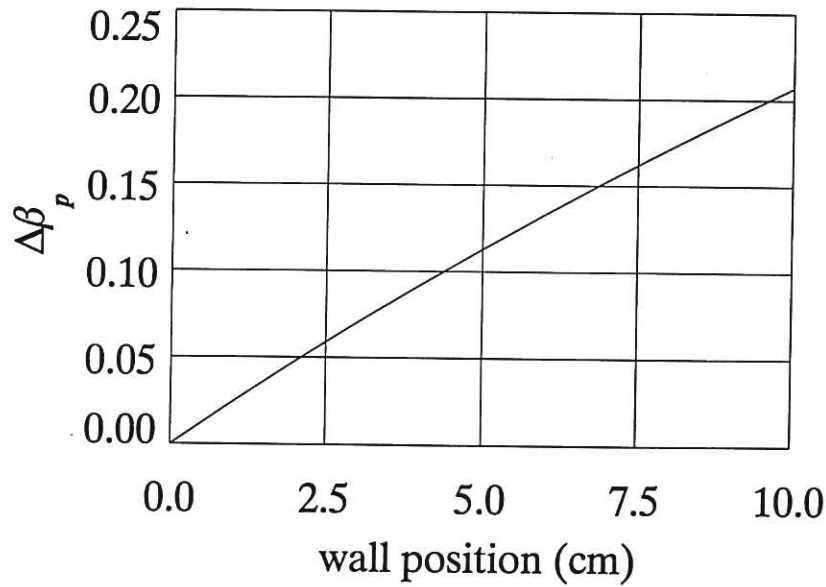


Figure 8. Calculated variation of β_p as a function of position of an ideal wall with respect to the inner surface of the actual resistive wall.

This value of axial- q is reasonable since the discharge is sawtoothing at this time. In

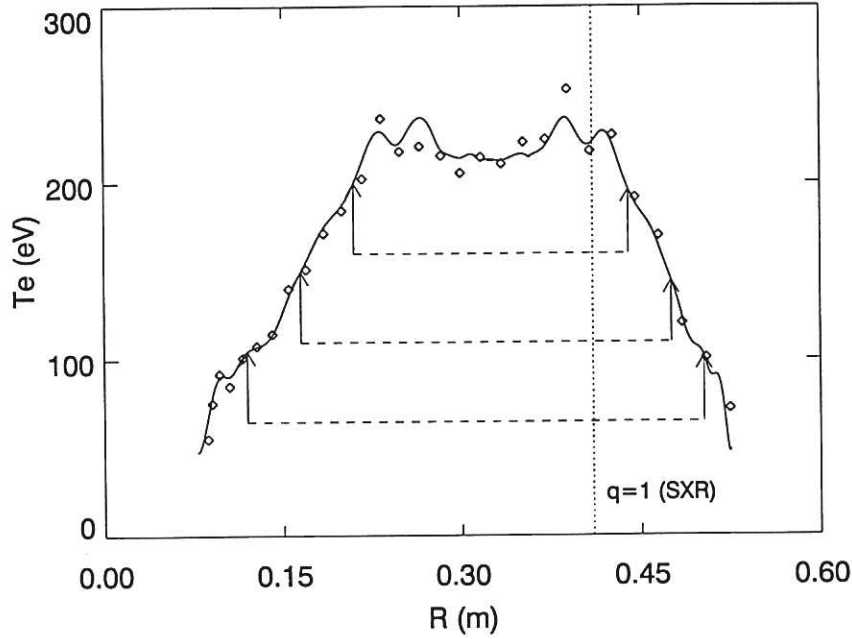


Figure 9. The radial T_e profile obtained from Thomson scattering for discharge 36429 (\diamond). The solid line shows the mapped flux surface locations from the EFIT reconstructions. The long-dashed lines show the locations of the relational constraints used to constrain EFIT and the short-dashed lines shows the location of the $q=1$ surface as inferred from the SXR.

addition, both the location of the outboard edge of the $q=1$ surface at $R=40.6\text{cm}$ and the position of the magnetic axis at $R_{mag} = 32.7\text{cm}$ are consistent with the SXR data. Figure 14 shows the EFIT computed pressure profile and the measured electron pressure profile. Assuming the dominant impurity is carbon, and the ion and electron temperatures are equal (this is indicated by the single charge exchange measurement), provides an estimate of effective charge, Z_{eff} consistent with the measured total thermal pressure, $Z_{eff} = \frac{7p_e - 6p_i}{p_e} \simeq 2$.

5. Discussion

The EFIT algorithm has been extended to enable the poloidal flux at multiple locations within the plasma to be constrained, to provide a robust method for including the radial profile of T_e obtained from Thomson scattering.

A model to account for flux diffusion through the START wall has been developed. The model is based on linear superpositions of solutions of the 1-D diffusion equation and is valid for times smaller than the resistive decay time of the wall. Calculations have shown that the effect of finite diffusion into the vessel could increase β_t by around 8%.

Reconstructions obtained using magnetic data and relational constraints between flux surfaces have demonstrated that β_t values can be obtained to within a fractional error of $\pm 10\%$. The fit to magnetic signals alone does not constrain q_0 ; however, by including constraints on the internal flux surface locations, the principle of constraining q_0 has been demonstrated. In the present instance the stringent accuracy requirements on the relational constraints means that they cannot be used to provide information on the value of q_0 . The use of just the poloidal flux contours in the con-

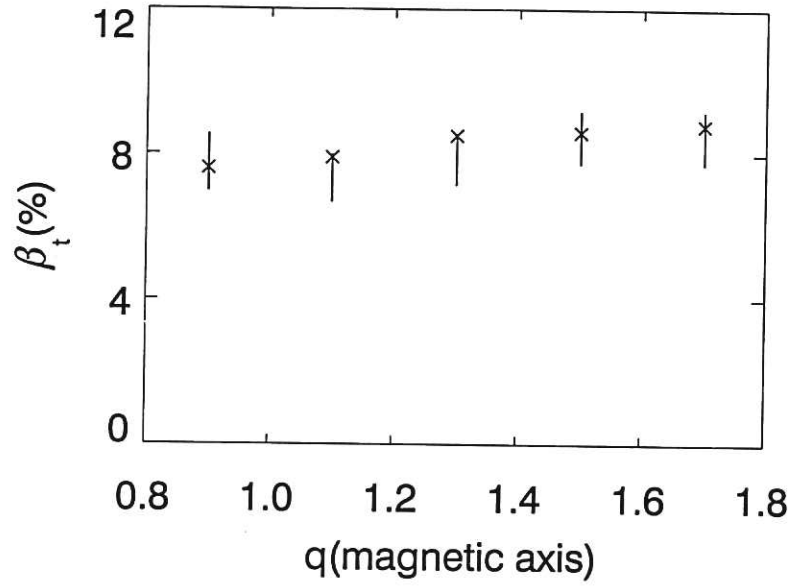


Figure 10. Results of EFIT reconstructions for discharge 36429 showing the variation of β_t with q_0 when the inboard and outboard fluxes are constrained to be equal at 3 pairs of points as shown in figure 10. Superimposed are error bars of results obtained with 2% Gaussian noise applied to the magnetic data.

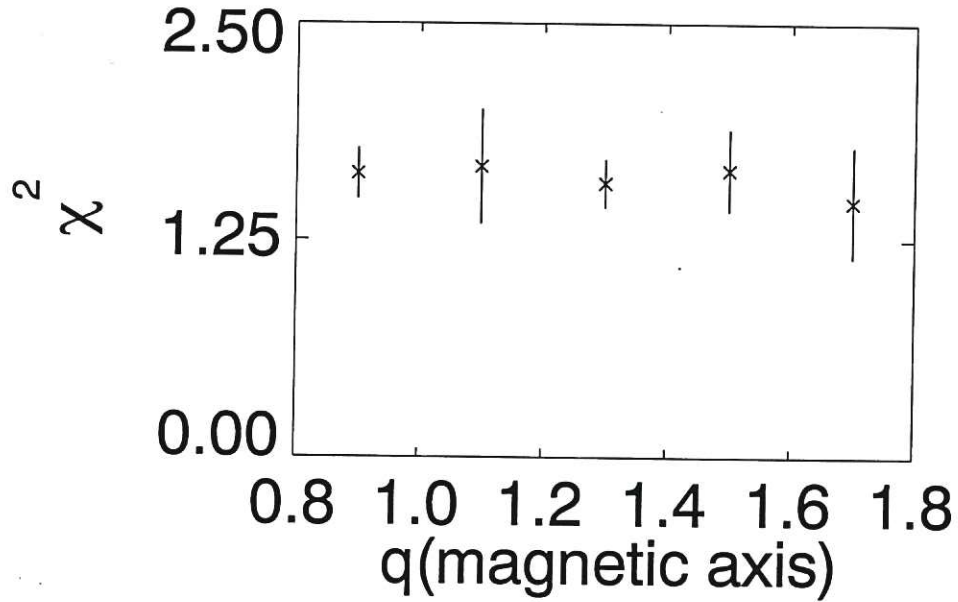


Figure 11. Results of EFIT reconstructions for discharge 36429 with 2% Gaussian noise applied to the magnetic data. The graph plots the variation of χ^2 from the magnetic signals, showing its insensitivity to q_0 .

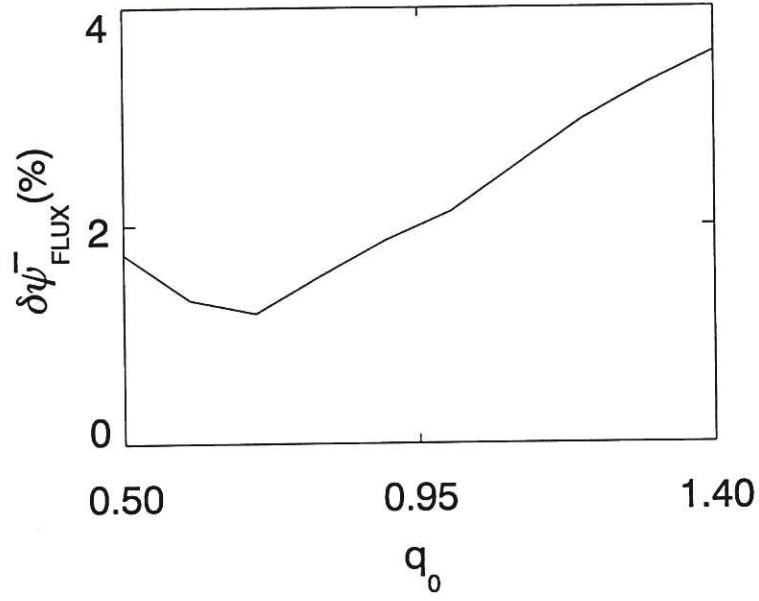


Figure 12. Result showing the discrepancy in poloidal flux values at the internal constraint locations for discharge 36429

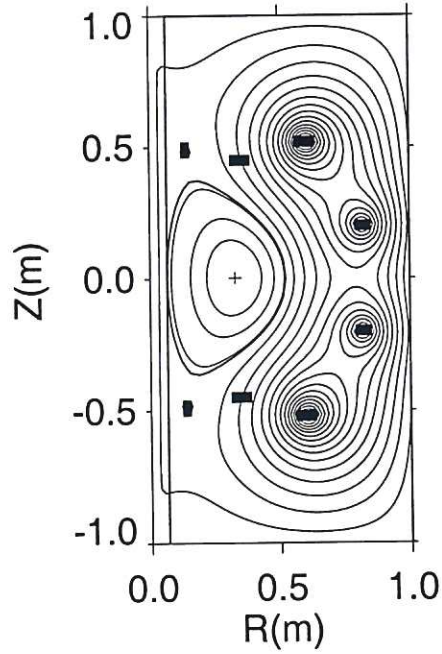


Figure 13. Reconstructed poloidal flux contours for discharge 36429

finement region and the total plasma current to fully define the equilibrium has been shown in previous work by Braams [25]. Expressions for the toroidal current density and q_0 in terms of the elongation of flux surfaces valid at large aspect ratio [26], suggest that additional measurements relating the poloidal flux values in a vertical plane

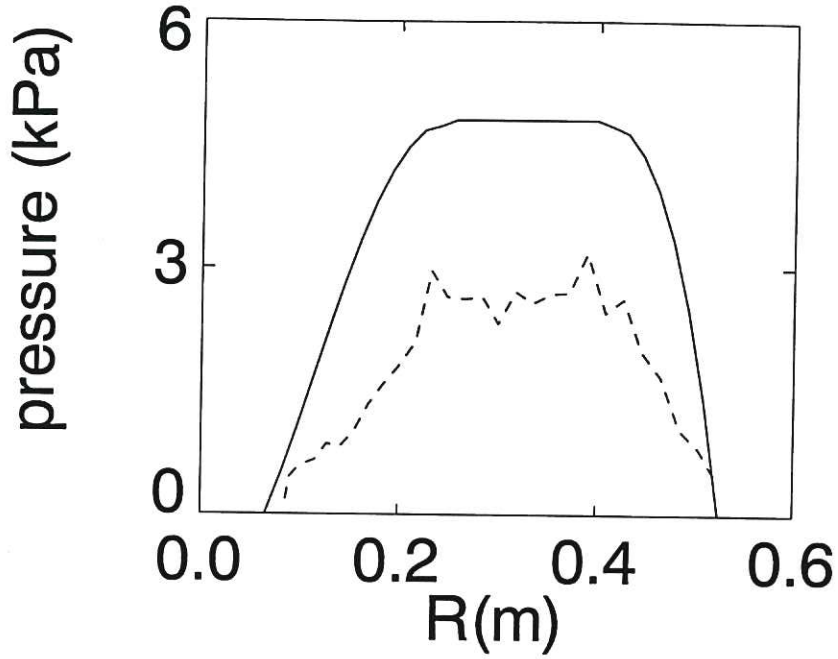


Figure 14. EFIT computed pressure profile on mid-plane (solid line) and electron pressure obtained from Thomson scattering (dashed lines).

(for example from a vertical T_e vertical profile) may also be beneficial. However, the sensitivity of q_0 to elongation of flux surfaces given in [26] suggests that additional measurements to constrain gradients in poloidal flux (i.e. poloidal magnetic field) are required to achieve accurate predictions on the q-profile.

Acknowledgements

The work was jointly funded by the UK Department of Trade and Industry and Euratom. The authors would like to thank Lang Lao for providing the EFIT code and for useful discussion; also Richard Martin, Neil Conway, Ian Jenkins and the START team for providing the experimental data.

n	C_n	$G(t)$	$\psi_p(x=0)$
-1/2	$\sqrt{\pi} = 1.77$	$\propto 1/\sqrt{t}$	constant
0	$2/\sqrt{\pi} = 1.13$	constant	$\propto 1/\sqrt{t}$
1/2	$\sqrt{\pi}/2 = 0.885$	$\propto \sqrt{t}$	$\propto t$
1	$4/(3\sqrt{\pi}) = 0.75$	$\propto t$	$\propto t^{3/2}$

Table 1. Values of C_n , $G(t)$ and $\psi_p(x=0)$ for several values of n .

Appendix A

A Analytical formulæ for flux diffusion

Simple formulae for the effective skin depth defined in equation (3.4) as

$$\delta = \frac{\psi_p(x=0)}{G} \quad (\text{A.1})$$

are given for the two regimes discussed in section 3.. For short time scales the wall appears infinitely thick. For long time scales the wall current is uniform across the wall and flux gradient (i.e. the magnetic field) at the outer edge of the wall is small and can be taken to be zero, provided the timescale is less than t_L given by equation (3.8).

Short time-scales: $0 < t < \sim 0.4\mu\sigma d^2$

A text-book solution for the poloidal flux at the surface of the wall [19, page 76] is

$$\psi_p(t) = \frac{1}{\sqrt{\pi\mu\sigma}} \int_0^t \frac{G(\tau)d\tau}{\sqrt{t-\tau}} \quad (\text{A.2})$$

If $G(t) = 0$ for $t < 0$, and then has a power-law variation $G(t) \propto t^n$ for $t > 0$

$$\delta(t) = C_n \sqrt{\frac{t}{\sigma\mu}} \quad (\text{A.3})$$

where C_n is a number depending on the index n in the power law for $G(t)$:

$$C_n = \frac{\Gamma(n+1)}{\Gamma(n+3/2)} \quad (\text{A.4})$$

where Γ is the gamma function. Table 1 gives values of C_n , $G(t)$ and $\psi_p(x=0)$ for particular values of n .

The case $n=0$ corresponds to equation (3.4). For large values of n , and even for these small ones, C_n is well approximated by the formula

$$C_n = \frac{1}{\sqrt{n+0.75}} \quad (\text{A.5})$$

Long time-scale: $\sim \mu\sigma d^2 < t < t_L$

For times long compared to the short time constant $\mu\sigma d^2$ (but short enough that external field leakage is still small), a formula for flux distribution in the wall can be given on the assumption that the applied field $G(t)$ varies slowly (i.e. varies by a small amount in a time $\mu\sigma d^2$). The wall has filled up with flux, which is now leaking across into the outside region. The solution is essentially an expansion in the small

parameter $\mu\sigma d^2 \partial/\partial t$ and with the notation $y = d - x$ takes the form

$$\begin{aligned}\psi_p(t, y) &= \frac{1}{\mu\sigma d} \int_0^t G(t) dt + dG(t) \left(\frac{y^2}{2d^2} - \frac{1}{6} \right) \\ &+ \mu\sigma d^3 \frac{\partial G(t)}{\partial t} \left(\frac{y^4}{24d^4} - \frac{y^2}{12d^2} + \frac{7}{360} \right) + \dots\end{aligned}\quad (\text{A.6})$$

The poloidal field component tangential to the wall at radius R is

$$B_p(t, y) = \frac{yG(t)}{Rd} + \frac{\mu\sigma d^2}{6R} \frac{\partial G(t)}{\partial t} \left(\frac{y^3}{d^3} - \frac{y}{d} \right) + \dots \quad (\text{A.7})$$

and the current density follows from substituting equation (A.6) for ψ_p into equation (3.2):

$$\begin{aligned}J(t, y) &= \frac{1}{\mu} \frac{\partial B_p(t, y)}{\partial y} \\ &= \frac{G(t)}{R\mu d} + \frac{\sigma d}{R} \frac{\partial G(t)}{\partial t} \left(\frac{y^2}{2d^2} - \frac{1}{6} \right) + \dots\end{aligned}\quad (\text{A.8})$$

These solutions show that to the lowest order the field distribution, $B_p(t, y)$, falls linearly from the wall value $G(t)$ inside to zero outside and the current distribution is uniform, as it would be in a steady-state layer. Time variation of the flux due to $G(t)$ gives rise to the next-order correction terms as it distorts the current profile and the field profile. Since the boundary conditions are that B_p is given at $y = 0$ and $y = d$, the values of B_p in the perturbation terms are zero at $y = 0$ and $y = d$ and the corresponding time-variation in total current $\int J(t, y) dy = 0$ although the spatial variation of $J(t, y)$ is non-uniform. This gives rise to results for the flux on the walls:

$$\psi_p(t, d) = \frac{1}{\mu\sigma d} \int_0^t G(t) dt + \frac{dG(t)}{3} \quad (\text{A.9})$$

$$\psi_p(t, 0) = \frac{1}{\mu\sigma d} \int_0^t G(t) dt - \frac{dG(t)}{6} \quad (\text{A.10})$$

or for the effective skin depth (substituting equation (A.9) into (A.1))

$$\delta = \frac{1}{G(t)\mu\sigma d} \int_0^t G(t) dt + \frac{d}{3} \quad (\text{A.11})$$

The first term in these expressions is essentially the time integral of the electric field $E = j/\sigma = G(t)/(R\mu\sigma d)$ required to drive the uniform current in the wall. Compared to an infinitely thin wall ($d \rightarrow 0$, but σd kept fixed) the extra flux leakage is as though the wall has moved out by a distance $d/3$, not $d/2$, as one might have suspected. The factor $1/3$ is for the case of zero B outside and depends in general on the ratio of B at the inner and outer surfaces.

The formula for the effective skin depth when $\delta(t) \propto t^n$ in this long time-scale regime, corresponding to equation (A.3) in the short time-scale regime, is:

$$\delta(t) = \frac{t}{(n+1)\mu\sigma d} + \frac{d}{3} \quad (\text{A.12})$$

For intermediate times $0.4 < t/\mu\sigma d^2 < 1$, the skin depth can be estimated by interpolation between the two formulae. The time-dependence for the case $n=0$ is shown in figure 1.

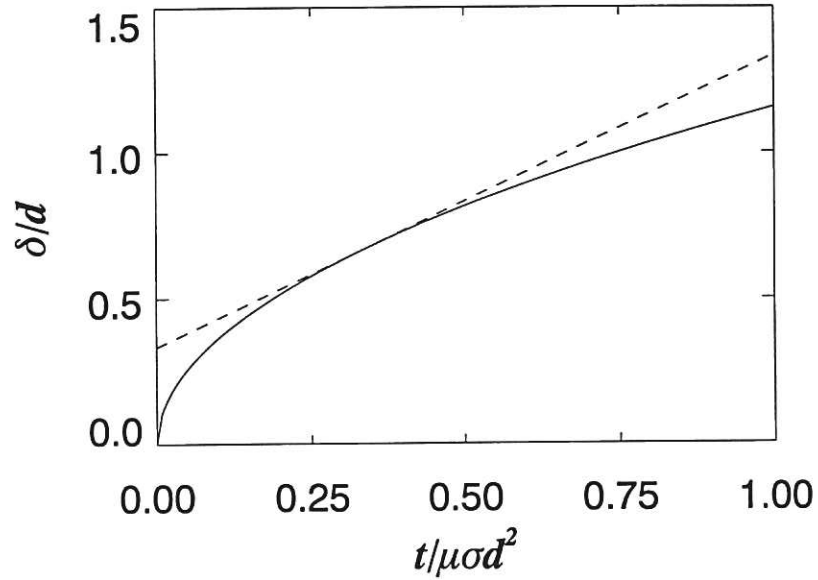


Figure 1. Time variation of skin-depth for $n = 0$ for short time-scales (solid line), and longer time-scales (dashed line). With this choice of n , the curves touch at $t/\mu\sigma d^2 = 1/3$.

References

- [1] LUXON, J.B., BROWN, B.B., Nuclear Fusion, 22 (1982) 813.
- [2] LAO, L.L., St. JOHN, H., STAMBAUGH, R.D., KELLMAN, A.G., PFEIFFER, W., Nuclear Fusion, 25 (1985) 1611.
- [3] BRAAMS, B.J., JILGE, W., LACKNER, K., Nuclear Fusion, 26 (1986) 699.
- [4] KUZNETSOV, Yu.K. PYATOV, V.N., YASIN, I.V., Sov J Plasma Phys, 13 (1987) 75.
- [5] HOFMANN, F., TONETTI, G., Nuclear Fusion, 28 (1988) 1871.
- [6] BLUM, J., LAZZARO, E., O'ROURKE, J., KEEGAN, B., STEPHAN, Y., Nuclear Fusion, 30 (1990) 1475.
- [7] ALLADIO, F., MICOZZI, P., Nuclear Fusion, 35 (1995) 305.
- [8] COOPER, W.A., WOOTTON, A.J., Plasma Physics, 24 (1982) 1183.
- [9] SALBERTA, E.R., GRIMM, R.C., JOHNSON, J.L., MANICKAM, J., TANG, W.M., Phys Fluids, 30 (1987) 2796.
- [10] IACONO, R., BONDESON, A., TROYON, F., GRUBER, R., Phys Fluids B 2 (1990) 1794.
- [11] MORSE, P and FESHBACH, H., "Methods of theoretical physics", McGraw-Hill, 1953.
- [12] LAO, L.L. *et al.*, Nuclear Fusion, 30 (1990) 1035.
- [13] O'BRIEN, D.P. *et al.*, Nuclear Fusion, 32 (1992) 1351.
- [14] SYKES, A. *et al.*, Nuclear Fusion, 32 (1992) 694.
- [15] WALSH, M.J., CONWAY, N.J., DUNSTAN, M., FORREST, M.J., HUXFORD, R.B., Rev of Scientific Instruments, 70 (1999) 742.
- [16] CONWAY, N.J., CAROLAN, P.G., TOURNIANSKI, M.R., Rev of Scientific Instruments, 70 (1999) 934.
- [17] CLINE, A.K., Communications of the Association for Computing Machinery, 17 (1974) 218.
- [18] PRESS, W. FLANNERY, B.P., TEUKOLSKY, S.A., VETTERLING, W.T., "Numerical recipes", Cambridge Univeristy Press, 1989.
- [19] CARSLAW, C.J and JAEGER, J.C., "Conduction of heat in solids", 2nd edition, 1959, OUP.

- [20] JACKSON, J., "Classical Electrodynamics", John Wiley, 1975.
- [21] AKERS, R., *to be submitted to Nuclear Fusion*
- [22] SYKES, A., *et al.*, Phys Rev Lett 84 (2000) 495.
- [23] SHAFRANOV, V.D., in "Reviews of Plasma Physics", Volume 2, Consultants Bureau, New York, 1966.
- [24] BATEMAN, G. "MHD Instabilities", MIT Press, 1978.
- [25] BRAAMS, B.J., Max-Planck-Institut fur Plasmaphysik, Report IPP5/2, 1985.
- [26] CHRISTIANSEN, J.P., CALLEN, J.D., ELLIS, J.J., Nuclear Fusion, 29 (1989) 703.

